RESEARCH ARTICLE | MAY 02 2023

Characterization of liquid flow and electricity generation in a glass channel based evaporation-driven electrokinetic energy conversion device **⊘**

Naoki Yanagisawa; Victor Dominguez; Sakur Mahmud; Debashis Dutta 🗷 👵





Physics of Fluids 35, 053604 (2023) https://doi.org/10.1063/5.0147235





Citation

CrossMark





Characterization of liquid flow and electricity generation in a glass channel based evaporation-driven electrokinetic energy conversion device

Cite as: Phys. Fluids **35**, 053604 (2023); doi: 10.1063/5.0147235 Submitted: 20 February 2023 · Accepted: 20 April 2023 · Published Online: 2 May 2023







Naoki Yanagisawa, Victor Dominguez, Sakur Mahmud, and Debashis Dutta^{a)} 🙃

AFFILIATIONS

Department of Chemistry, University of Wyoming, Laramie, Wyoming 82071, USA

a) Author to whom correspondence should be addressed: ddutta@uwyo.edu. Fax: (307) 766-2807

ABSTRACT

Evaporation-driven spontaneous capillary flow presents a promising approach for driving electrolytes through electrically charged channels and pores in electrokinetic energy conversion devices. However, there are no literature reports of detailed flow visualization in these systems and/or experimental observations relating the liquid velocity and evaporation rate to the generated voltage and current. In this manuscript, we describe such a visualization study for a glass channel based electrokinetic energy conversion device with one of its channel terminals left open to ambient air for facilitating the evaporation process. Fluorescence microscopy was used to measure the liquid velocity in the electrokinetic energy conversion channel by observing the advancement of an electrolyte solution dyed with a neutral tracer. The accumulation of the same dye tracer was also imaged at the open terminal of this glass conduit to estimate the rate of solvent evaporation, which was found to be consistent with the flow velocity measurements. Additionally, an electrochemical analyzer was employed to record the electrical voltage and current produced by the device under different operating conditions. The highest electrical power output was derived in our experiments upon flowing de-ionized water through a 1 μ m deep channel, which also produced the fastest liquid velocity in it. Moreover, the energy conversion efficiency of our device was observed to increase for shallower channels and lower ionic strength electrolytes, consistent with previous literature reports on electrokinetic energy conversion platforms.

Published under an exclusive license by AIP Publishing. https://doi.org/10.1063/5.0147235

I. INTRODUCTION

It has been long known that pressure-driven flow of an electrolyte through a conduit/pore with a net electrical surface charge generates an electrical current (streaming current). This streaming current arises due to the migration of counter-ions residing within the Debye layer formed around the solid–liquid interfaces in the system.¹ A charge separation is automatically realized under these conditions, which produces a voltage drop across the channel/pore terminals that can be utilized to perform electrical work.^{2–4} Initial studies on characterizing this electrokinetic energy conversion phenomenon focused on the use of mechanical pumps to drive the electrolytic liquid through well-defined conduits that yielded moderate energy conversion efficiencies.^{5–7} Such conversion of mechanical to electrical power was substantially improved in subsequent research works by transporting the electrolyte solution through highly charged nanoporous membranes.^{8–12} Remarkably, these investigations also showed that significant open circuit potentials (OCPs) could be

generated in both nanochannel and nanopore based electrokinetic energy conversion platforms using water as the flowing electrolyte, which is both non-hazardous and abundant in nature. Nevertheless, it was simultaneously recognized that the external work required to drive liquid flow in these devices limits their practical utility for generating electrical power. Additionally, the need for carrying considerable amounts of electrolyte in the system and a mechanical pump or pressurized vessel to drive the electrolyte flow compromises their portability.

The above limitations for electrokinetic energy conversion devices have been addressed by our laboratory¹³ and others^{14–16} in more recent studies in which the requirement of an external pump or pressurized vessel was eliminated by driving the electrolyte using spontaneous capillary flow. The noted liquid flow was sustained in these spontaneous electrokinetic energy conversion devices (SEECDs) by evaporating the solvent at an open channel/pore terminal extracting heat from the environment without the need for any external work.

Open circuit potentials ranging from several hundred millivolts to a few volts have been regularly reported for SEECDs since their inception, employing a variety of porous films as the evaporating sur-Moreover, it has been shown that the electrical output of these devices can be improved by exposing the vaporizing solvent to solar radiation, airflow, or low grade heat dissipated by external sources, which accelerated the evaporation process. 22,23 Condensation and recycling of the evaporating solvent have been also demonstrated for closed SEECDs, significantly improving the portability of these systems.²⁴ Interestingly, the strategy of solvent condensation can be employed to simultaneously produce clean water during evaporationdriven electrokinetic energy conversion using an aqueous electrolyte, which is particularly relevant to desalination applications.²⁵ The influence of different electrode materials on the electrical performance of SEECDs was further characterized in a recent publication under different operating conditions. 26 Notably, this report showed galvanic corrosion to significantly improve the electrical power generated by electrokinetic energy devices for appropriate electrode-electrolyte combinations. In addition, the above work demonstrated that the gas phase composition, e.g., oxygen content, around the electrodes can substantially influence the voltage and current generated by an

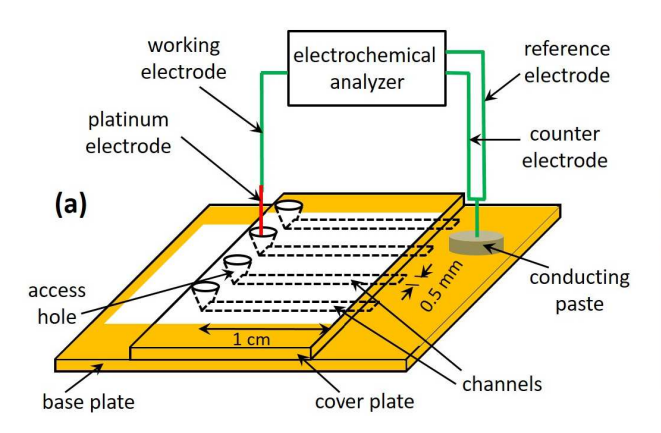
Although several materials and operational strategies have been explored in the literature for enhancing the performance of evaporation-driven electrokinetic energy conversion devices, there has been limited effort made for quantitatively understanding liquid transport and solvent evaporation rates in these systems. A comprehensive understanding of these processes, however, is key to establishing the scaling principles for SEECDs that can guide their optimal design and operation.²⁷ In this article, we contribute to this research need by presenting a visualization study of liquid transport and solvent evaporation rates in a glass channel based SEECD. Fluorescence microscopy was used to image the liquid flow in our device as well as the solvent loss from the open channel terminal employing an aqueous electrolyte with a solubilized dye tracer. Additionally, the electrical voltage and current generated by the device was measured using an electrochemical analyzer to characterize its electrokinetic energy conversion performance. The energy conversion efficiency of our platform was observed to increase for shallower channels and lower ionic strength electrolytes, consistent with previous literature reports on electrokinetic energy conversion systems. A maximum electrical power output of 612 pW was measured for our device upon flowing de-ionized (DI)

water through a $1 \mu m$ deep conduit, which also produced the fastest spontaneous capillary flow velocity under the conditions chosen for this study.

II. EXPERIMENTAL PROCEDURE

A. Device fabrication

For fabricating the fluidic devices employed in this work, bottom and cover plates made from borosilicate glass were purchased from Telic Company (Valencia, CA). While the purchased cover plates had both their faces unprotected, the bottom ones came with a thin layer of chromium and photoresist laid down on one of their surfaces. Custom designed photomasks created through Fineline Imaging, Inc. (Colorado Springs, CO) were used to pattern the desired channel layout onto the bottom plate using standard photolithographic methods.^{28,29} Four parallel channels (see Fig. 1) were patterned on the bottom plate with all of the conduits being 1.5 cm long and 500 μ m wide. After completion of the photo-patterning process, the photoresist layer was cured in a microposit developer MF-319 (Rohm and Haas), and the chromium layer was removed along the channel network with a chromium etchant (Transene, Inc.). The fluidic ducts were then etched to a depth between 0.3 and 3 μ m using a buffered oxide etchant (Transene, Inc.). Note that the cross sections of the channels with different depths were uniform but had a surface roughness in the range of 5-20 nm (root mean square height) introduced by the wet-etching process. The protective photoresist and chromium layers on the bottom plate were subsequently removed using the MF-319 and chromium etchant solutions, respectively. Finally, the channels were sealed off by first bringing a glass cover plate in contact with the baseplate in de-ionized water and then allowing the two to bond at $550\,^{\circ}\text{C}$ for 12 h in a furnace. While one end of these sealed conduits was accessed by punching a 1 mm diameter hole on the cover plate using a microabrasive blasting system (Vaniman Manufacturing Co.) prior to the bonding process, the other end terminated well beyond the edge of the cover plate, and was, therefore, open to the atmosphere [see Fig. 1(a)]. During the bonding step, it was ensured that the wet-etched channels extended at least 0.5 mm beyond the left edge of the 1 mm access hole, and their axes aligned with the center of the corresponding circular opening. Also, the cover plate used was about 5 cm long and 1.5 cm wide and was bonded such that channel length from the right edge of the access hole to its open end was 1 cm. This alignment left just over 3 mm of the wet-etched channel exposed



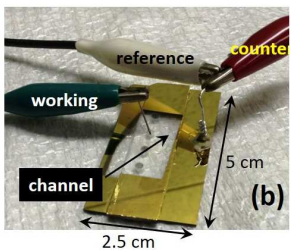


FIG. 1. (a) Schematic of the electrokinetic energy conversion device described in this manuscript. (b) An image of the electrokinetic energy conversion device used in this work. The yellow regions in subfigures (a) and (b) correspond to the chromium/gold layer deposited on the glass plate using a dual metal evaporator system for making electrical contact with the open channel terminal.

to the ambient air beyond the right edge of the cover plate. The bottom plate was chosen to be 5 cm long and 2.5 cm wide in all our devices. To allow electrical contact with the liquid at the open channel terminal, this region was coated with metal layers. For the coating process, a dual metal evaporator system (Energy Beam Sciences, Inc.) was used to sequentially deposit a 130 nm layer of chromium followed by a 40 nm layer of gold, employing procedures previously reported by our laboratory.^{32–34} The channels and a small region around them were masked with adhesive tapes during the coating step, however, to maintain optical transparency needed for the dye visualization process. These masking tapes were later removed before the flow visualization experiments, yielding the device shown in Fig. 1(b).

B. Device operation

The electrokinetic energy conversion channel was prepared for an experiment by filling it with methanol through the access hole, applying a high pressure (\sim 1.03 bar relative to the atmosphere pressure) at this location. The conduit was then rinsed with 0.1M NaOH, de-ionized (DI) water, and the relevant electrolyte in that order for 15 min each using the same procedure. Most of the liquid drained at the open channel edge during the rinsing step was removed using a vacuum pump, and this area later dried with a tissue paper. The access hole was subsequently filled with about $2 \mu l$ of DI water/electrolyte and the system left undisturbed for at least 5 min to allow the device to reach a steady state. The reason for introducing a small volume of liquid, i.e., $2 \mu l$, into the access hole was to minimize the hydrostatic head at this location.³⁵ For prolonged experiments, this liquid volume was replenished with 2 μ l of DI water/electrolyte every 15 min to maintain a steady liquid flow in the electrokinetic energy conversion channel. Only one channel in the device was used for an experiment at a time with the remaining ones left dry over that period. The air temperature around the electrokinetic conversion device was regulated using an electric radiant heater and monitored with a thermometer.³⁶ The humidity around the device was recorded using a hygrometer. All voltage and current measurements were made by electrically connecting the working electrode of an electrochemical analyzer (CH Instruments, Inc.) to the electrolyte in the access hole using a platinum wire. At the same time, the reference and the counter electrodes of this analyzer were shorted and connected to the open edge of the channel using an electrically conducting paste (Chemtronics, catalog# CW7100) placed on the gold layer as shown in Figs. 1(a) and 1(b). For visualizing liquid flow in the electrokinetic energy conversion channel, rhodamine B samples were prepared in DI water or an aqueous solution containing potassium chloride (KCl). The fluorescence measurements were made using an epifluorescence microscope (Nikon) with appropriate bandpass excitation (528-543 nm) and emission (590-650 nm) optical filters. The fluorescence images were recorded using an EMCCD camera (Andor) and analyzed with the ImageJ software. The grayscale levels recordable by our camera varied in the range of 0-65 535. The camera exposure time was chosen to be 50 ms for the evaporation rate measurements with a 1.2x signal gain.

III. RESULTS AND DISCUSSION

A. Flow characterization

To visualize the reported evaporation-driven capillary flow, our device was first operated for 5 min to allow it to attain a steady state following the introduction of $2\,\mu l$ of the relevant electrolyte in the

appropriate access hole. Most of the remaining liquid was then pipetted out from this hole and replaced with $2 \mu l$ of the same electrolyte containing 10 µM of the rhodamine B dye. The liquid flow velocity was subsequently measured by tracing the advancement of the stained electrolyte front 3-8 mm upstream of the open channel terminal. Notice that the flow of rhodamine B in our device was unrelated to capillary filling of empty micro-/nanoducts³⁷ as it occurred in a channel that had already been filled out with a dye-free electrolyte. In Fig. 2(a), we have included a series of fluorescence images that depict the advancement of the dyed electrolyte front through a 1 μ m deep conduit due to the evaporation-driven capillary flow, which were acquired using a 10× objective. Later, similar images were taken using a $4\times$ objective to trace the dyed electrolyte front over a larger length scale yielding the data included in Fig. 2(b). In this figure, the position of dyed electrolyte front was assumed to be the axial location where the fluorescence intensity averaged over the channel width attained a value halfway between that recorded for a conduit completely filled with the dyed and undyed electrolytes. The figure shows a linear increase in the distance migrated by the front with time, establishing a steady operating state for our device. The migration rate of the advancing solution was determined to be 473 μ m/s for these measurements at the ambient temperature (25 ± 1 °C) and relative humidity $(27.1\% \pm 3.0\%)$ chosen for our experiments. This velocity was also observed to be nearly independent of the KCl concentration in the liquid at least for the dilute electrolytes used in the study. Note that the rate of advection reported for rhodamine B in the above figure is over three orders of magnitude faster than its diffusive transport in water around room temperature. Based on a diffusion coefficient of 3.6×10^{-6} cm²/s reported for rhodamine B in water at $21.5 \,^{\circ}$ C, 38 it is estimated that that this dye would require about 7×10^4 s to advance its front by 5 mm. In Fig. 2(c), the dependence of the liquid velocity (u) on channel depth (d) was assessed for DI water and the 0.1 mM KCl solution, which showed u to reach a relatively sharp maximum at $d=1\,\mu\mathrm{m}$ for both the chosen liquids. However, the volumetric flow rate corresponding to these velocity measurements was seen to rise monotonically with an increase in d leveling off to a value of about 0.4 nL/s for conduits deeper than 2 μ m. The pressure-drop across the electrokinetic energy conversion channel was estimated from these velocity measurements as $\Delta P = 12\eta Lu/d^2$, and was seen to decrease monotonically for deeper channels. The ΔP values included in Fig. 2(d) were computed assuming a 1 cm long channel, i.e., L = 1 cm, and liquid viscosity (η) values reported in the literature for the relevant experimental conditions.³

The above observations indicate that the evaporation-driven capillary flow in our system was determined by a balance between the pressure-differential across the liquid–air interface and solvent vaporization rate at the open channel terminal. Specifically, this transport process was governed by the first factor in channels shallower than 1 μ m and the second one in deeper conduits. The plateauing of the volumetric flow rate (q) in conduits deeper than 1 μ m, for example, is indicative of evaporation-limited transport. This hypothesis is also supported by the fact that the value to which q leveled off increased with the air temperature around the open channel terminal. Additionally, its magnitude of about 0.5 nL/s under these conditions compares well with literature reports of evaporation rates at open microchannel terminals. 40,41 For channels shallower than 1 μ m on the other hand, the effect of temperature on the liquid velocity was

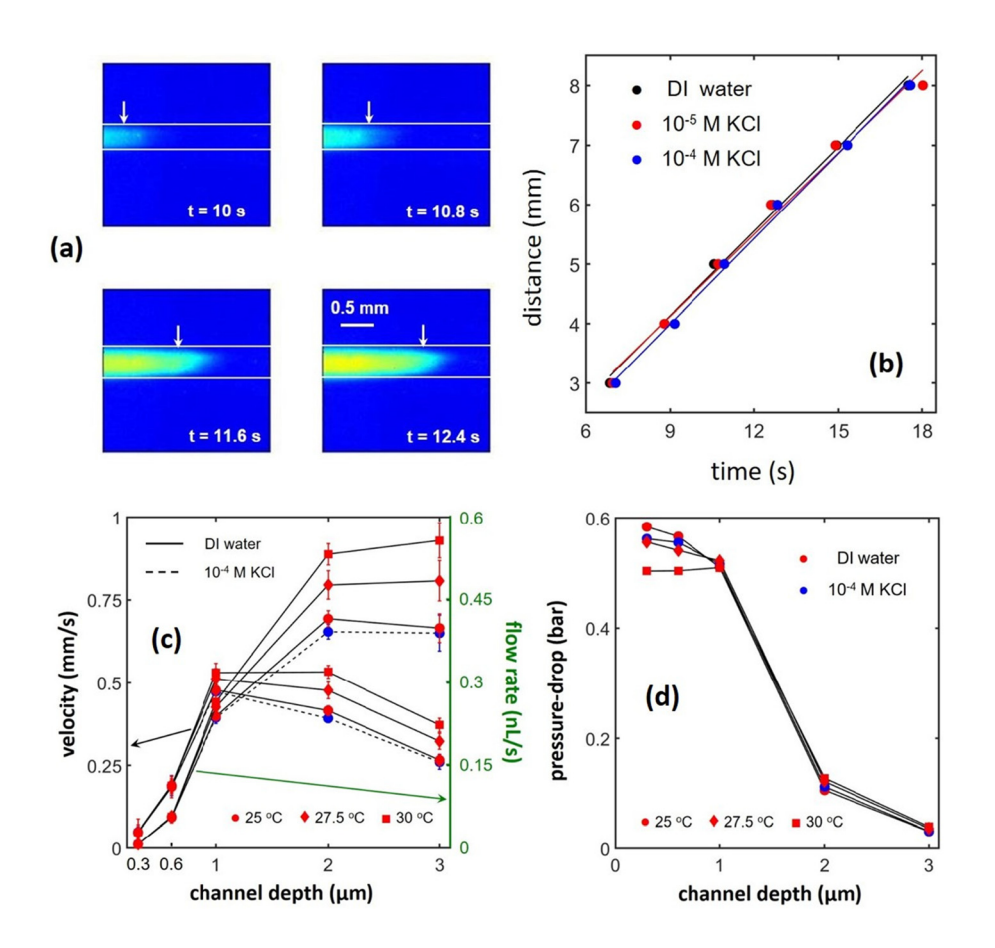


FIG. 2. (a) Fluorescence image of a traveling rhodamine B front in a $1 \mu m$ deep channel advected by evaporation-driven spontaneous capillary flow. The images were obtained using a 10 $\mu \rm M$ rhodamine B solution prepared in de-ionized water. (b) Distance traveled by the rhodamine B front in a 1 μ m deep glass channel as a function of time. (c) Observed variation in the liquid velocity with channel depth. The error bars in these data correspond to ± 1 standard deviation (68% confidence interval) and were estimated based on five independent measurements. The volumetric flow rates included in the sub-figure were determined by multiplying the reported liquid velocity with the channel cross-sectional area. (d) Pressure-drop across the glass channel as predicted by the Hagen-Poiseuille equation when applied to the flow measurements included above.

minimal and the pressure-drop across the channel plateaued for decreasing values of d. In this regime, ΔP likely determined the liquid flow rate but then was not seen to increase with a reduction in the channel depth. This observation was surprising as we had expected the smaller radii of curvature at the liquid-air interface determining ΔP to be controlled by the channel depth. Visualization of this interface, however, suggested that the surface roughness of the glass plate at the open channel terminal may have rather dictated the liquid-air interface curvature in our devices for channels shallower than 1 μ m. This occurred because the glass plates used in our experiments were cut by first scoring them with a carbide tip followed by snapping them along the scored line, which produced a surface roughness on the order of $1 \, \mu \text{m}$ at the cut edges. The jagged edges of the bottom plate also prevented the characterization of the liquid-air interface in the current study as no reliable images of this interface could be obtained for our device. Noticeably, ΔP leveled off to values in the range of 0.5–0.6 bar for $d < 1 \,\mu\text{m}$ in Fig. 2(d), which compares well with the ratio γ/r when γ equals the surface tension of water (72 mN/m at 25 °C) and r (presumably the surface roughness at the open channel end) is assigned a value of 1.25 μ m. The surface roughness referred to here originated from the jagged edges of the bottom plate in our device and was unrelated to that introduced by the wet-etching process. Moreover, the noted pressure-drop was also seen to decrease for higher air temperatures around the open channel terminal consistent with the expected reduction in the magnitude of γ in warmer

environments. We would like to point out here that although this study did not involve flow measurements with different liquids, higher viscosities have been shown to slow down evaporation-driven capillary flow. ^{42,43} Additionally, the efficiency of electrokinetic energy conversion devices has been reported to decrease for viscous liquids, suggesting them to be sub-optimal for practical applications. ^{6,7}

B. Solvent evaporation measurements

The rate of solvent evaporation at the open channel terminal was estimated in our work by imaging the accumulation of rhodamine B dye in this region. The noted accumulation occurred due to dye transport into this area by spontaneous capillary flow and its subsequent buildup as a result of solvent removal by evaporation. It must be noted that the devices used for this study did not have any metal coating on the glass plates as that interfered with the visualization of the reported dye accumulation process. In Fig. 3(a), we have included images showing the accumulation of rhodamine B at the edge of a 1 μ m deep channel and the corresponding increase in the observed fluorescence intensity with time. Now assuming that the liquid volume in which the dye concentration occurred (V_c) remains constant over the observation period, the rate of solvent evaporation (q_e) may be estimated by applying a mass balance on the dye species to yield the expression

$$q_e = V_c \frac{d}{dt} \left(\frac{I}{I_0} \right), \tag{1}$$

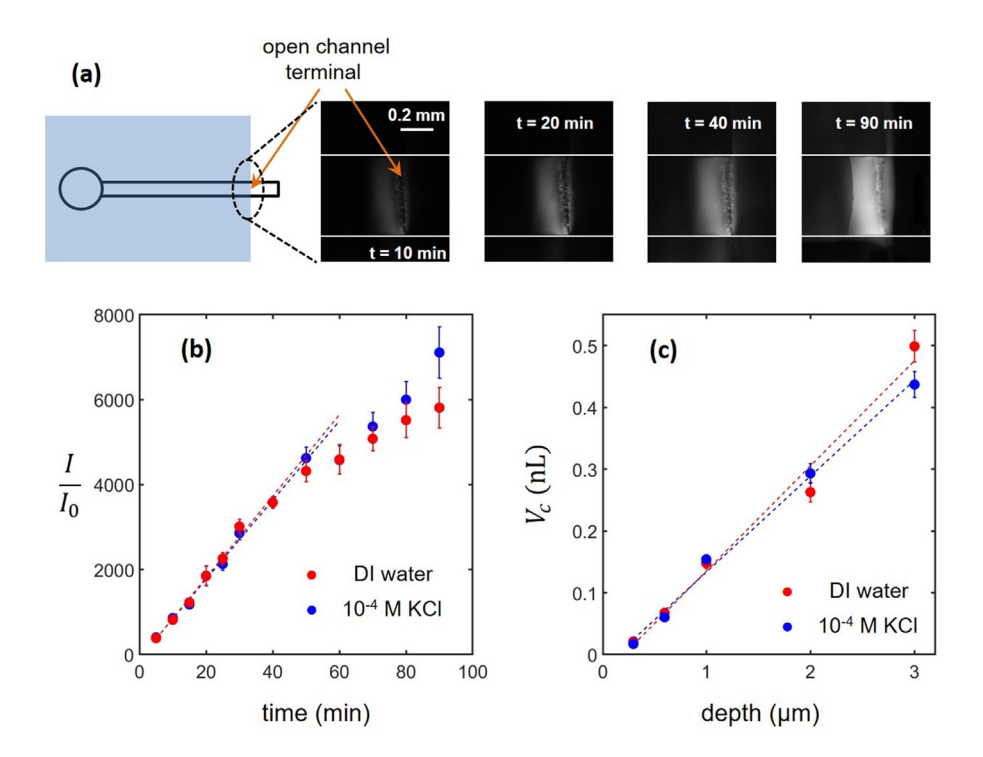


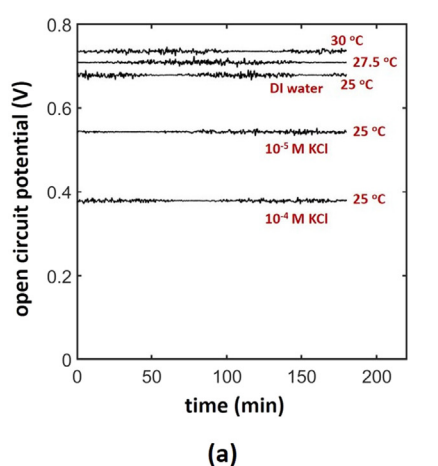
FIG. 3. (a) Schematic of the open channel terminal and fluorescence images showing the accumulation of rhodamine B in this region. The images were obtained by flowing a 0.1 μ M rhodamine B solution prepared in de-ionized water through a 1 μm deep channel. (b) Observed temporal variation in the relative fluorescence intensity (I/I_0) recorded around the open terminal of a 1 μ m deep channel at 25 °C. The symbols I and I_0 in the above ratio denote the average fluorescence intensities in the dye concertation region and channel area far away from the open terminal, respectively. The dotted curves represent the best-fitted line to the first eight data points included in the sub-figure. (c) Estimated liquid volume in which rhodamine B accumulated around the open channel terminal as determined by Eq. (1) for the different channel depths used in this study. The error bars in these data correspond to ±1 standard deviation (68% confidence interval) and were calculated based on five independent measurements.

where I and I_0 denote the average fluorescence intensities in the dye concertation region and channel area far away from the open terminal, respectively. In Fig. 3(b), the recorded temporal variation in I/I_0 has been presented showing a linear increase in this ratio with time at least over the first 50 min of observation. The rate of increase in the fluorescence signal was then seen to slow down beyond this period likely due to self-quenching of the dye or other non-idealities in the system. The steady rate of increase observed for I/I_0 during the initial period of our experiment supports the proposed hypothesis of a constant volume in which rhodamine B accumulated due to solvent evaporation. Moreover, this volume was estimated to be about 0.15 nL for a 1 μ m deep channel, which is obtained by substituting the volumetric flow rate reported in Fig. 3(c) for q_e in Eq. (1). This number can be put into perspective by assuming that the entire volume in which the dye concentration occurred resided within the glass channel. In that situation, the dye accumulation region would extend about 300 μm into the conduit from its open terminal, which is consistent with the images included in Fig. 3(a). The validity of the physical model described by Eq. (1) was further assessed in our study by examining the dependence of V_c on channel depth. Figure 3(c) shows a linear increase in this quantity with d, which further justifies our assumption of a constant V_c during the initial period of dye accumulation. Finally, it must be pointed out that the temporal variation in I/I_0 shown in Fig. 3 was found to be similar for DI water and the 0.1 mM KCl solution as was the case for the liquid velocity recordings included Sec. III A. For the experiments described in Fig. 3, all measurements were made using a $0.1 \,\mu\text{M}$ rhodamine B solution prepared in the appropriate electrolytic medium that presumably produced dye concentrations of about 1 mM around the channel edge after 90 min of operation. Note that this concentration level was still substantially below the solubility limit of rhodamine B in water, which has been reported to be around 16 mM,

and, therefore, should not have caused any dye precipitation during our measurements. It must be pointed out that the dye accumulation region appears noticeably different after an hour of device operation (e.g., at $t=90\,\mathrm{min}$), which we suspect is a result of changes in the liquid flow field around the open channel edge at high dye concentrations due to alterations in liquid viscosity, surface tension, hydrophobicity of the channel surface caused by adsorption of dye molecules onto its walls, etc. Also, note that the I_0 value for the images included in Fig. 3(a) was typically in the range of 6–8. This value was the average fluorescence intensity recorded far away from the open channel edge where dye accumulation occurred. Moreover, for the images included in Figs. 2 and 3, we did not utilize the allowed detection range of the camera. Thus, it should be possible to improve the quality of our measurements by optimizing the camera settings, which will be performed for our future research works on this topic.

C. Electrical measurements

Having established the evaporation-driven spontaneous capillary flow in our device, we proceeded to assess its ability to generate electrical power. To this end, we first investigated the stability of the electrical energy output by the device over a timescale on the order of several hours. In Fig. 4(a), we have included data obtained from these measurements that were performed in a 1 μ m deep channel using deionized water or a KCl solution as the electrolyte medium. The figure shows that the open circuit potential (OCP) recorded for our glass channel had a standard deviation of less than 3% of its mean value for over 3 h, demonstrating the temporal stability in its electrical performance. The noted OCP was also found to be higher for decreasing KCl concentrations in the electrolyte, yielding a value of about 0.68 V for de-ionized water at 25 °C. Moreover, this voltage increased to



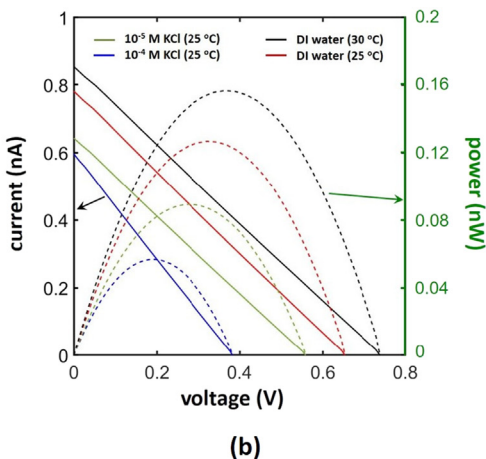


FIG. 4. (a) Temporal variation in the open circuit potential value recorded for a 1 μ m deep channel over a period of 3 h. (b) Observed relationship between the voltage and current (solid lines) output for a 1 μ m deep channel. By definition, the x- and y- intercepts in this sub-figure correspond to the open circuit potential and short circuit current in the device. The electrical power in the sub-figure (dotted lines) was computed as the product of the measured voltage and current.

about 0.73 V upon raising the air temperature around the open channel terminal to 30 °C. In Fig. 4(b), we have presented the electrical current measured at the terminals of the glass channel as a function of the voltage developed across it for a 1 μ m deep channel. By definition, the x- and y- intercepts in this figure corresponded to the open circuit potential and short circuit current (SCC) in the device. The figure shows a linear variation between the recorded current and voltage, with the slope of the curve representing the reciprocal of the electrical resistance of the glass channel. For the 1 µm deep channel, SCCs on the order of 1 nA were observed, which corresponded to a resistance value of just under 1 G Ω when DI water and the 0.01 mM KCl solution was used as the electrolyte. This electrical resistance was seen to decrease by about 30% for the 0.1 mM KCl solution but did not change by any measurable amount when the air temperature around the open channel terminal was increased to 30 °C. Figure 4(b) also shows the electrical power produced by the glass channel, which was computed as the product of the measured voltage and current. This quantity attained a maximum value of 1/4 (OCP × SCC) when the output voltage and current equaled half their respective maxima. The dependence of the open circuit potential and short circuit current on the channel depth was investigated in Fig. 5(a), which shows that their magnitudes were maximized in the $1 \mu m$ deep channel. This

observation is consistent with the velocity measurements included in Fig. 2 as the streaming potential is known to increase with the liquid flow speed in the system. 45 The decrease in OCP and SCC for d $> 1 \,\mu\mathrm{m}$ was observed to be sharper than the reduction in liquid velocity, however, as the Debye layer occupied a smaller fraction of the channel in deeper conduits. The maximum electrical power generated by our energy conversion platform has been included in Fig. 5(b), which expectedly showed a similar dependence on channel depth as the OCP and SCC values. Additionally, the electrical resistance of our glass channels (R) has been reported in this sub-figure, which was computed as the ratio OCP/SCC. These resistance values showed a monotonic decrease in their magnitude with d leveling off in the submicrometer deep channels. The weak dependence of R on channel depth, particularly in shallow conduits filled with dilute electrolytes as noted above, is consistent with literature reports of surface conductance governing the electrical resistance of shallow glass channels.⁴⁶ The negligible change in R observed upon increasing the air temperature around the open channel terminal to 30 °C is somewhat surprising nevertheless, and is indicative of the fact that most of the electrolyte within the channel may have been still at the room temperature of 25 °C even upon warming the air around the open channel terminal.

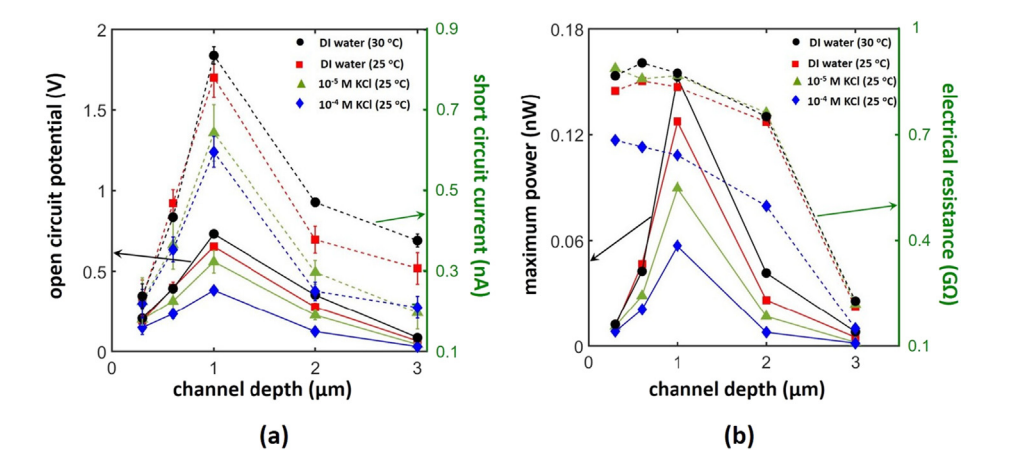


FIG. 5. (a) Observed variation in the open circuit potential (OCP, solid lines) and short circuit current (SCC, dotted lines) produced by the reported electrokinetic energy conversion device. The error bars in these data correspond to ± 1 standard deviation (68% confidence interval) and were estimated based on five independent measurements. (b) Maximum electrical power output from our device (solid lines) computed as $1/4\,(\text{OCP}\times\text{SCC})$ and its electrical resistance (dotted lines) estimated as the ratio OCP/SCC.

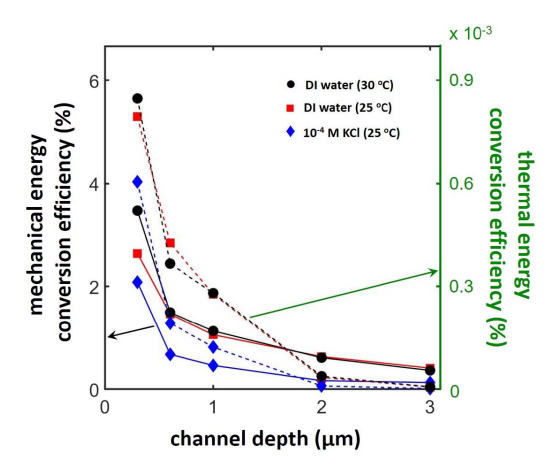


FIG. 6. Estimated mechanical (solid lines) and thermal (dotted lines) energy conversion efficiencies for the reported device as a function of the different channel depths used in this study. These mechanical and thermal energy conversion efficiencies were estimated as the ratio of the maximum electrical power output from the device over the rate of energy used to drive the liquid flow and evaporate the solvent, respectively.

Finally, the energy conversion efficiency of our glass channel has been assessed in Fig. 6 for the different channel depths used in the study. This efficiency was estimated as the ratio of the maximum electrical power output from the device over the rate of mechanical or thermal energy used to drive the liquid flow or evaporate the solvent. The mechanical power input into the system was computed as ΔPq_e for these estimations, and the corresponding thermal power was assumed to be $-\Delta G_V q_e$. In the above expression, ΔP , q_e , and ΔG_V refer to the pressure-drop across the channel length, solvent evaporation rate at the open channel terminal on a volumetric basis, and Gibbs free energy of vaporization per unit volume of water at the relevant temperature, respectively. The numerical value for the noted Gibbs free energy was arrived at using the equation $\Delta G_V = \Delta G_V^o + RT \ln [P_{H_2O(g)}]$, where $\Delta G_V^o = 8.43 \,\mathrm{kJ/mol}$ denotes the standard Gibbs free energy of vaporization for water, and $P_{H_2O(g)}$ equals the product of the relative humidity and saturation vapor pressure of H₂O in the atmosphere. Figure 6 shows that both the noted energy conversion efficiencies decreased with the channel depth in a similar manner, which occurred due to a reduction in the volume fraction occupied by the Debye layer in the system.^{6,7,45} The efficiencies were also lower for the solution with a higher KCl concertation in both cases for the same reason. Moreover, the mechanical energy driving the electrolyte flow was estimated to be converted at an efficiency of a few percent in agreement with previous literature reports. However, the conversion of thermal power into electricity was observed to be over three orders of magnitude less efficient.

IV. CONCLUSIONS

In conclusion, the above study demonstrates the utility of fluorescence visualization methods for measuring liquid velocity and solvent evaporation rates in evaporation-driven electrokinetic energy conversion devices. The measurements obtained for these quantities were found to be consistent with each other and previous literature reports, establishing their validity. Electroosmotic flow was neglected in the current analysis as its contribution was estimated to be only about 1%

of the evaporation-driven capillary flow in our system. However, in situations when electroosmotic flow is significant, the local electric field in the conduit may be determined employing liquid velocity measurements. The above study further establishes a simple approach for measuring the solvent evaporation rate at an open channel terminal. Although the liquid volume in which the tracer molecules accumulated due to this solvent loss appeared to be unchanging during the initial period of our experiments, the mechanistic details of this concentration process are unclear and may be explored using particle velocimetry methods. Interestingly, the outlined measurements also offer a simple approach for visualizing the accumulation of solubilized and dispersed matter in evaporation-driven electrokinetic energy conversion devices. Measurements of electrical voltage and current reported in this study were observed to be consistent with the fluorescence visualization data and showed that the conversion of thermal energy into electricity in the system was highly inefficient. This finding is particularly significant as it indicates the possibility of realizing substantially faster liquid flows through the electrokinetic energy conversion channel for a given evaporation rate at the open channel terminal. To explore this possibility, our laboratory is currently generating thermal maps of the region around the evaporating solvent interface to comprehensively understand heat transport in the system with the aspiration of improving the thermal energy conversion efficiency in evaporation-driven electrokinetic energy conversion devices.

ACKNOWLEDGMENTS

D.D. acknowledges funds from the National Science Foundation (No. CHE-1808507) and the Wyoming NASA Space Grant Consortium (NASA Grant No. 80NSSC20M0113) for carrying out some of the experiments included in this manuscript.

AUTHOR DECLARATIONS Conflict of Interest

The authors have no conflicts to disclose.

Author Contributions

Naoki Yanagisawa: Data curation (equal); Investigation (equal), Methodology (equal); Validation (equal); Visualization (equal). Victor Dominguez: Formal analysis (equal); Validation (equal); Visualization (equal), Sakur Mahmud: Investigation (equal); Methodology (equal); Validation (equal); Visualization (equal), Debashis Dutta: Conceptualization (equal); Data curation (equal); Formal analysis (equal); Funding acquisition (equal); Investigation (equal); Methodology (equal); Project administration (equal); Supervision (equal); Writing – original draft (equal); Writing – review & editing (equal).

DATA AVAILABILITY

The data that support the findings of this study are available from the corresponding author upon reasonable request.

REFERENCES

¹J. F. Osterle, "Electrokinetic energy conversion," J. Appl. Mech. 31, 161-164

- ²W. Olthuis, B. Schippers, J. Eijkel, and A. Van Den Berg, "Energy from streaming current and potential," Sens. Actuators, B 111–112, 385–389 (2005).
- ³B. Fan, A. Bhattacharya, and P. R. Bandaru, "Enhanced voltage generation through electrolyte flow on liquid-filled surfaces," Nat. Commun. 9, 4050 (2018).
- ⁴A. M. Duffin and R. J. Saykally, "Electrokinetic power generation from liquid water microjets," J. Phys. Chem. C 112, 17018–17022 (2008).
- ⁵A. Mansouri, S. Bhattacharjee, and L. Kostiuk, "High-power electrokinetic energy conversion in a glass microchannel array," Lab Chip 12, 4033–4036 (2012).
- ⁶F. H. J. van der Heyden, D. J. Bonthuis, D. Stein, C. Meyer, and C. Dekker, "Electrokinetic energy conversion efficiency in nanofluidic channels," Nano Lett. 6, 2232–2237 (2006).
- ⁷F. H. J. van der Heyden, D. J. Bonthuis, D. Stein, C. Meyer, and C. Dekker, "Power generation by pressure-driven transport of ions in nanofluidic channels," Nano Lett. 7, 1022–1025 (2007).
- ⁸A. Bentien, T. Okada, and S. Kjelstrup, "Evaluation of nanoporous polymer membranes for electrokinetic energy conversion in power applications," J. Phys. Chem. C 117, 1582–1588 (2013).
- ⁹B. S. Kilsgaard, S. Haldrup, J. Catalano, and A. Bentien, "High figure of merit for electrokinetic energy conversion in Nafion membranes," J. Power Sources 247, 235–242 (2014).
- ¹⁰S. Haldrup, J. Catalano, M. R. Hansen, M. Wagner, G. V. Jensen, J. S. Pedersen, and A. Bentien, "High electrokinetic energy conversion efficiency in charged nanoporous nitrocellulose/sulfonated polystyrene membranes," Nano Lett. 15, 1158–1165 (2015).
- ¹¹S. Haldrup, J. Catalano, M. Hinge, G. V. Jensen, J. S. Pedersen, and A. Bentien, "Tailoring membrane nanostructure and charge density for high electrokinetic energy conversion efficiency," ACS Nano 10, 2415–2423 (2016).
- ¹²R. Qu, X. Zeng, L. Lin, G. Zhang, F. Liu, C. Wang, S. Ma, C. Liu, H. Miao, and L. Cao, "Vertically-oriented Ti₃C₂T_x MXene membranes for high performance of electrokinetic energy conversion," ACS Nano 14, 16654–16662 (2020).
- ¹³D. Dutta, "Electrical energy generation in fluidic channels and membranes using spontaneous capillary flow," U.S. patent 10,944,123 (2021).
- ¹⁴G. Xue, Y. Xu, T. Ding, J. Li, J. Yin, W. Fei, Y. Cao, J. Yu, L. Yuan, L. Gong, J. Chen, S. Deng, J. Zhou, and W. Guo, "Water-evaporation-induced electricity with nanostructured carbon materials," Nat. Nanotechnol. 12, 317–321 (2017).
- ¹⁵C. Li, K. Liu, H. Liu, B. Yang, and X. Hu, "Capillary driven electrokinetic generator for environmental energy harvesting," Mater. Res. Bull. **90**, 81–86 (2017).
- ¹⁶T. G. Yun, J. Bae, A. Rothschild, and I. D. Kim, "Transpiration driven electrokinetic power generator," ACS Nano 13, 12703–12709 (2019).
- 17 T. Ding, K. Liu, J. Li, G. Xue, Q. Chen, L. Huang, B. Hu, and J. Zhou, "All-printed porous carbon film for electricity generation from evaporation-driven water flow," Adv. Funct. Mater. 27, 1700551 (2017).
- ¹⁸G. Zhang, Z. Duan, X. Qi, Y. Xu, L. Li, W. Ma, H. Zhang, C. Liu, and W. Yao, "Harvesting environment energy from water-evaporation over free-standing graphene oxide sponges," Carbon 148, 1–8 (2019).
- ¹⁹Z. Sun, L. Feng, X. Wen, L. Wang, X. Qin, and J. Yu, "Ceramic nanofiber-based water-induced electric generator," ACS Appl. Mater. Interfaces 13, 56226–56232 (2021).
- ²⁰T. Tabrizizadeh, J. Wang, R. Kumar, S. Chaurasia, K. Stamplecoskie, and G. Liu, "Water-evaporation-induced electric generator built from carbonized electrospun polyacrylonitrile nanofiber mats," ACS Appl. Mater. Interfaces 13, 50900–50910 (2021).
- ²¹K. Saha, J. Deka, and K. Raidongia, "Extraction of evaporation-driven electrokinetic streaming potential from V₂O₅ nanochannels through secondary sources," ACS Appl. Energy Mater. 4, 8410–8420 (2021).
- ²²S. Fang, W. Chu, J. Tan, and W. Guo, "The mechanism for solar irradiation enhanced evaporation and electricity generation," Nano Energy 101, 107605 (2022).
- ²³G. Zhang, Y. Xu, Z. Duan, W. Yu, C. Liu, and W. Yao, "Conversion of low-grade heat via thermal-evaporation-induced electricity generation on nano-structured carbon films," Appl. Therm. Eng. 166, 114623 (2020).

- ²⁴K. Liu, T. Ding, J. Li, Q. Chen, G. Xue, P. Yang, M. Xu, Z. L. Wang, and J. Zhou, "Thermal-electric nanogenerator based on the electrokinetic effect in porous carbon film," Adv. Energy Mater. 8, 1702481 (2018).
- 25 H. Peng, D. Wang, and S. Fu, "Unidirectionally driving nanofluidic transportation via an asymmetric textile pump for simultaneous salt-resistant solar desalination and drenching-induced power generation," ACS Appl. Mater. Interfaces 13, 38405–38415 (2021).
- ²⁶T. Tabrizizadeh, Z. She, K. Stamplecoskie, and G. Liu, "Empowerment of water-evaporation-induced electric generators via the use of metal electrodes," ACS Omega 7, 28275–28283 (2022).
- ²⁷A. Yaroshchuk, "Evaporation-driven electrokinetic energy conversion: Critical review, parametric analysis and perspectives," Adv. Colloid Interface Sci. 305, 102708 (2022).
- ²⁸D. C. S. Bien, P. V. Rainey, S. J. M. Mitchell, and H. S. Gamble, "Characterization of masking materials for deep glass micromachining," J. Micromech. Microeng. 13, S34–S40 (2003).
- ²⁹N. Yanagisawa and D. Dutta, "Kinetic ELISA in microfluidic channels," Biosensors 1, 58–69 (2011).
- ³⁰C. J. Wadsworth, N. Yanagisawa, and D. Dutta, "Nanochannel arrays as supports for proton exchange membranes in microfluidic fuel cells," J. Power Sources 195, 3636–3639 (2010).
- ³¹L. Xia and D. Dutta, "High efficiency hydrodynamic chromatography in microand sub-micrometer deep channels using an on-chip pressure-generation unit," Anal. Chim. Acta 950, 192–198 (2017).
- 32T. F. Kinde and D. Dutta, "A microfluidic SPLITT device for fractionating low-molecular weight samples," Anal. Chem. 85, 7167–7172 (2013).
- 33T. F. Kinde, T. D. Lopez, and D. Dutta, "Electrophoretic extraction of low molecular weight cationic analytes from sodium dodecyl sulfate containing sample matrices for their direct electrospray ionization mass spectrometry," Anal. Chem. 87, 2702–2709 (2015).
- 34T. F. Kinde, N. Hess, and D. Dutta, "Enhancement in MS-based peptide detection by microfluidic free-flow zone electrophoresis," Electrophoresis 41, 545–553 (2020).
- 35 J. Pena, S. J. McAllister, and D. Dutta, "A glass microchip device for conducting serological survey of West Nile viral antibodies," Biomed. Microdevices 16, 737, 743 (2014)
- ³⁶N. Yanagisawa, J. O. Mecham, R. C. Corcoran, and D. Dutta, "Multiplex ELISA in a single microfluidic channel," Anal. Bioanal. Chem. 401, 1173 (2011).
- 37D. Yang, M. Krasowska, C. Priest, M. N. Popescu, and J. Ralston, "Dynamics of capillary-driven flow in open microchannels," J. Phys. Chem. C 115, 18761–18769 (2011).
- ³⁸S. A. Rani, B. Pitts, and P. S. Stewart, "Rapid diffusion of fluorescent tracers into *Staphylococcus epidermidis* biofilms visualized by time lapse microscopy," Antimicrob. Agents Chemother. 49, 728–732 (2005).
- ³⁹R. B. Bird, W. E. Stewart, and E. N. Lightfoot, *Transport Phenomena*, 2nd ed. (John Wiley & Sons, Inc., 2007).
- ⁴⁰N. S. Lynn, C. S. Henry, and D. S. Dandy, "Evaporation from microreservoirs," Lab Chip 9, 1780–1788 (2009).
- ⁴¹N. S. Lynn and D. S. Dandy, "Passive microfluidic pumping using coupled capillary/evaporation effects," Lab Chip 9, 3422–3429 (2009).
- ⁴²P. Kolliopoulos, K. S. Jochem, R. K. Lade, Jr., L. F. Francis, and S. Kumar, "Capillary flow with evaporation in open rectangular microchannels," Langmuir 35, 8131–8143 (2019).
- ⁴³P. Kolliopoulos, K. Jochem, L. Francis, and S. Kumar, "Capillary flow of evaporating liquid solutions in open rectangular microchannels," J. Fluid Mech. 938, A22 (2022).
- ⁴⁴CRC Handbook of Chemistry and Physics, 72nd ed., edited by D. R. Lide (CRC Press, Boca Raton, FL, 1991–92).
- 45D. Dutta, "Solutal transport in rectangular nanochannels under pressuredriven flow conditions," Microfluid. Nanofluid. 10, 691–696 (2011).
- ⁴⁶D. Stein, M. Kruithof, and C. Dekker, "Surface-charge-governed ion transport in nanofluidic channels," Phys. Rev. Lett. 93, 035901 (2004).